Journal of ELECTRONIC MATERIALS, Vol. 43, No. 8, 2014
DOI: 10.1007/s11664-014-3161-y

Mid-Wavelength Infrared *n*B*n* for HOT Detectors

A. ROGALSKI[1,2] and P. MARTYNIUK[1,3]

1.—Institute of Applied Physics, Military University of Technology, 2 Kaliskiego Street, 00-908 Warsaw, Poland. 2.—email: rogan@wat.edu.pl. 3.—e-mail: pmartyniuk@wat.edu.pl

Recently, new strategies to achieve high-operating-temperature (HOT) detectors have been proposed, including barrier structures such as *n*B*n* devices, unipolar barrier photodiodes, alternative materials such as superlattices, and multistage (cascade) infrared devices. In the case of *n*B*n* detectors, the barriers must be correctly engineered and correctly located in the device structure to achieve optimal performance. This paper presents the limitations of barrier unipolar devices and the progress in their development for HOT operation in the mid-wavelength infrared range. Their performance is compared with state-of-the-art HgCdTe photodiodes.

Key words: Unipolar barrier detectors, *n*B*n* detectors, InAsSb ternary alloy, InAs/GaSb type II superlattices, HgCdTe photodetectors

INTRODUCTION

A number of concepts to improve mid-wavelength infrared (MWIR) detector performance and reach high-operating-temperature (HOT) conditions have been effectively implemented. Initial efforts were concentrated on photoconductors and photoelectromagnetic detectors.[1,2] Subsequently, several ways to achieve HOT detector operation have been elaborated, including nonequilibrium detector design with Auger suppression and optical immersion.[2] Recently, new strategies used to achieve HOT detectors include barrier structures such as *n*B*n*, unipolar barrier photodiodes, alternative materials such as superlattices (SLs), and multistage (cascade) infrared devices.[3,4] Auger generation–recombination (GR) can be limited by designing detectors with materials inherently exhibiting lower Auger GR rates, amongst which InAs/GaSb type II superlattices (T2SLs) should be listed.[3] Another method to reduce the detector's dark current is to reduce the volume of detector material using the photon-trapping detector concept.[4]

In the case of large infrared (IR) focal-plane arrays (FPAs), raising the detector's operating temperature has benefits in terms of reduced cooling power and increased lifetime, and enables an overall reduction in size, weight, and power (SWaP) for handheld applications. Low-power, large-format, small-pixel IR FPAs with large, dynamic, on-chip digital image processing and high-speed readout are now possible. At present, extraordinary HOT detector technologies that can perform at significantly elevated temperatures to minimize these trade-offs are being developed.

In 2006, a new type of heterostructure *n*B*n* device was proposed, in which no depletion layer exists in any active narrow-bandgap region.[5] Here "*n*" stands for the doping in identical narrow-gap semiconductors and "B" stands for an undoped central barrier layer. This device is similar to that proposed by White in 1983, in which two narrow-gap semiconductors surround a *p*-type wide-bandgap semiconductor and a barrier only exists in the conduction band.[6]

This paper presents the progress in the development of barrier infrared HOT detectors, presenting potential materials and barrier structures that eliminate the cooling requirements of photodetectors operating in the MWIR range.

BENEFITS AND LIMITATIONS OF UNIPOLAR BARRIER PHOTODETECTORS

Unipolar barrier photodetectors can be implemented in different semiconductor materials. Practical application has been demonstrated in InAs,[5,7] InAsSb,[8,9] and InAs/GaSb T2SLs,[10] and recently also in HgCdTe ternary alloy.[11,12]

(Received October 17, 2013; accepted April 1, 2014; published online April 30, 2014)

The introduction of unipolar barriers in various designs based on T2SLs drastically changed the architecture of infrared detectors. The term "unipolar barrier" was coined to describe a barrier that can block one carrier type (electron or hole) but allows unimpeded flow of the other (Fig. 1).

The *n*B*n* bandgap diagram is shown in Fig. 1d. The *n*-type semiconductor on one side of the barrier constitutes a contact layer for biasing the device, while the *n*-type narrow-bandgap semiconductor on the other side of the barrier is a photon-absorbing layer whose thickness should be comparable to the absorption length of light in the device, typically several microns. The barrier should be located near the minority-carrier collector and away from the region of optical absorption. Such a barrier arrangement allows photogenerated holes to flow to the contact (cathode) while the majority-carrier dark current, reinjected photocurrent, and surface current are blocked (Fig. 1e). So, the *n*B*n* detector is designed to reduce the dark current associated with Shockley–Read–Hall (SRH) processes without impeding the photocurrent (signal). In particular, the barrier serves to reduce the surface leakage current.

The *n*B*n* device somewhat resembles a typical *p*–*n* photodiode, except that the junction (space-charge region) is replaced by an electron-blocking unipolar barrier (B), and that the *p*-contact is replaced by an *n*-contact. It can be stated that the *n*B*n* design is a hybrid between a photoconductor and a photodiode.

The operating principles of *n*B*n* and related *X*B*n* detectors (where *X* stands for either *n*- or *p*-type contact layers) have been described in detail in the literature.[5,7,10,13–16] While the idea of the *n*B*n* design originated with bulk materials,[5,17] its demonstration using T2SL-based materials facilitates experimental realization of the *n*B*n* concept with improved control of band-edge alignments.[18] Unipolar barriers can also be inserted into the conventional *p*–*n* photodiode architecture.[7,13]

Figure 2 shows a typical Arrhenius plot of the dark current in a conventional diode and in a *n*B*n* detector. Because in the *n*B*n* detector there is no depletion region, the generation–recombination contribution to the dark current from the photon-absorbing layer

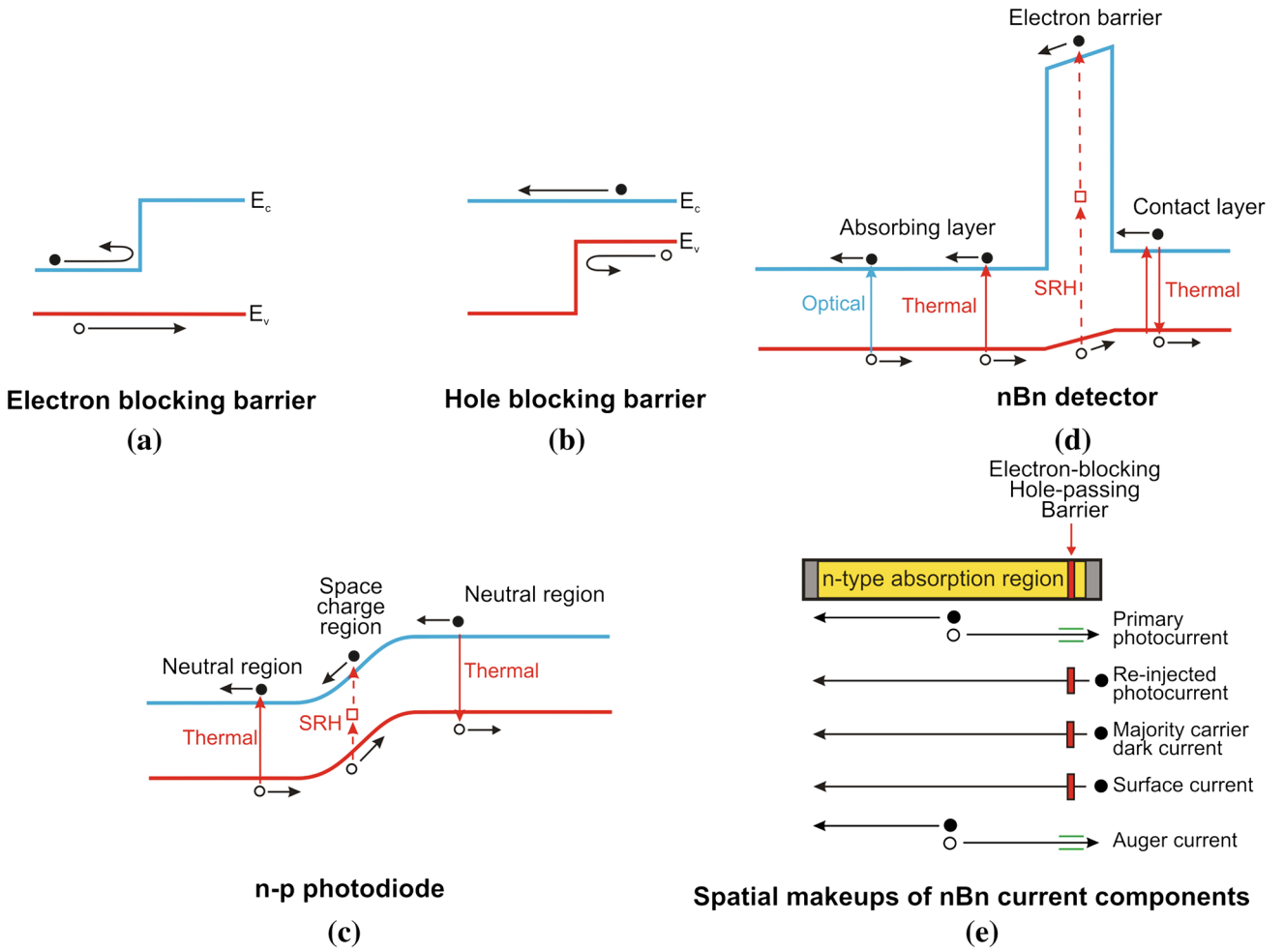

Fig. 1. Schematic illustrations of (a) electron- and (b) hole-blocking unipolar barriers, and (c) detector and *p*–*n* photodiode. (d) Bandgap diagram of *n*B*n* barrier. (e) Spatial makeup of the various current components and barrier blocking, adapted after Ref. 13.

is totally suppressed. The lower portion of the Arrhenius plot for the standard photodiode has a slope that is roughly half that of the upper portion. The solid line (*n*B*n*) is an extension of the high-temperature diffusion-limited region to temperatures below T_c. T_c is defined as the crossover temperature at which the diffusion and generation–recombination currents are equal. In a low-temperature region, the *n*B*n* detector offers two important advantages. First, it should exhibit a higher signal-to-noise ratio than a conventional diode operating at the same temperature. Second, it will operate at a higher temperature than a conventional diode with the same dark current. This is depicted by a dashed horizontal green line in Fig. 2.

Figure 3 shows an example of the photovoltaic detector family: the double heterostructure photodiode, and *p*M*p* and *p*B*n* barrier detectors. The *p*M*p* device consists of two *p*-doped superlattice active regions and a thin M-structure with higher energy barrier. The bandgap difference between the superlattice and M-structure falls in the valence band, creating a valence-band barrier for the majority holes in a *p*-type semiconductor.[19] In the case of the *n*B*p* structure, the *p*–*n* junction can be located at the interface between the heavily doped *p*-type material and the lower-doped barrier, or within the lower-doped barrier itself.[20] However, a key feature of the devices is the pair of complementary barriers, namely an electron barrier and a hole barrier, formed at different depths in the growth sequence. Such a structure is known as a complementary barrier infrared device (CBIRD) and was invented by Ting and others at the Jet Propulsion Laboratory (JPL).[21]

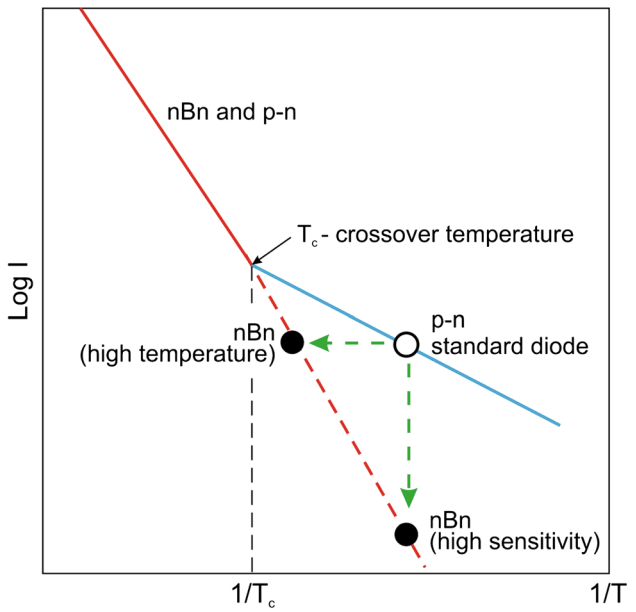

Fig. 2. Schematic Arrhenius plot of the dark current in a standard diode and in a *n*B*n* device (adapted after Ref. 14).

MATERIAL CONSIDERATIONS FOR *X*B*n* HOT DETECTORS

As mentioned above, a correct location of the barrier layer within the detector structure is essential to prevent blocking of photogenerated carriers by the barrier. The barrier should be located near the minority-carrier contact and far from the region of optical absorption. For material systems where a large conduction-band offset is not realizable, the *p*B*n* architecture may be preferable. The traditional *n*B*n* structure requires a bias to operate. When zero-bias operation is crucial, again the *p*B*n* architecture may be used.[22] Having a large band offset in one band and zero offset in the other is not the only requirement to fabricate an *X*B*n* detector; lattice matching between surrounding materials is also significant.

Currently, among the materials used in fabrication of *X*B*n* detectors, the 6.1-Å $A^{III}B^{V}$ family plays a decisive role, offering high performance combined with high design flexibility, direct energy gaps, and strong optical absorption. The three semiconductors InAs, GaSb, and AlSb form an approximately lattice-matched set around 6.1 Å, with room-temperature energy gaps ranging from 0.36 eV (InAs) to 1.61 eV (AlSb).[23] Like other semiconductor alloys, they are of interest principally for their heterostructures, especially when combining InAs with the two antimonides and their alloys. This combination offers band line-ups that are drastically different from those of the more widely studied AlGaAs system, being one of the principal reasons for interest in the 6.1-Å family. The most exotic line-up is that of InAs/GaSb heterojunctions, as discovered in 1977 by Sakaki et al.,[24] which exhibit a broken-gap line-up: at the interface, the bottom of the conduction band of InAs lines up below the top of the valence band of GaSb with a break in the gap of about 150 meV. In such a heterostructure, with partial overlap of the InAs conduction band with the GaSb-rich solid-solution valence band, electrons and holes are spatially separated and localized in self-consistent quantum wells formed on both sides of the heterointerface. This leads to unusual tunneling-assisted radiative recombination transitions and novel transport properties. As illustrated in Fig. 4, with the availability of type I (nested, or straddling), type II staggered, and type II broken-gap (misaligned, or type III) band offsets between the GaSb/AlSb, InAs/AlSb, and InAs/GaSb material pairs, respectively, there is considerable flexibility in forming a rich variety of alloys and superlattices.

From the viewpoint of producibility, $A^{III}B^{V}$ materials offer much stronger chemical bonds and thus greater chemical stability compared with HgCdTe. The 6.1-Å materials can be epitaxially grown on GaSb and GaAs substrates. In particular, 4-inch-diameter GaSb substrates became commercially available in 2009, offering improved economy of scale for fabrication of large-format FPAs.

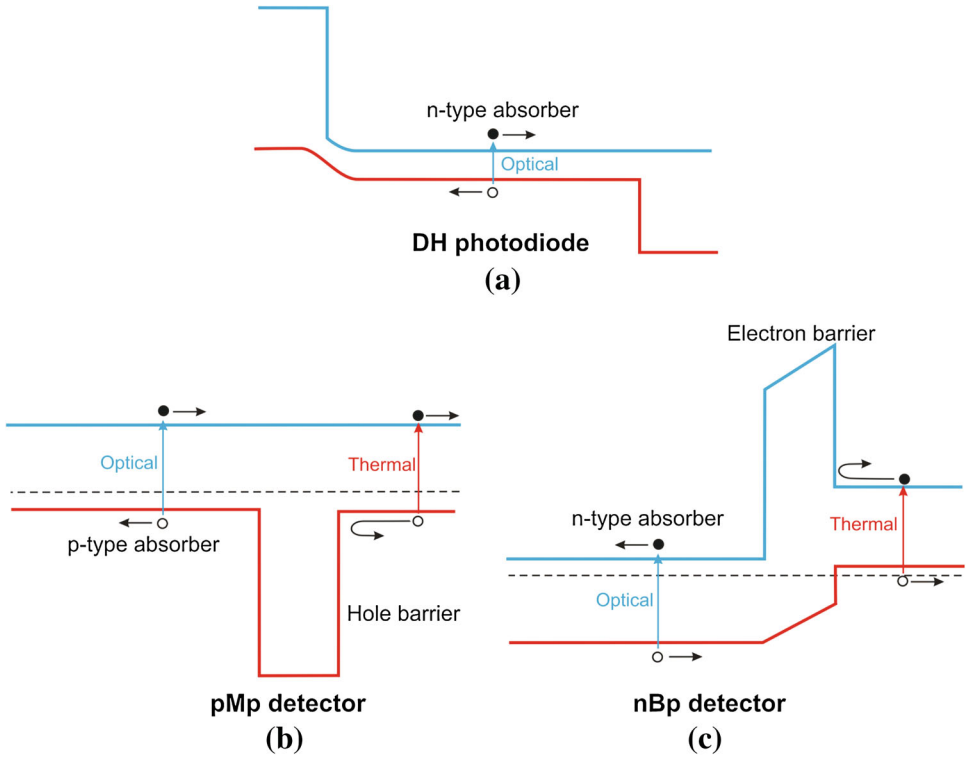

Fig. 3. Bandgap diagrams of photovoltaic detectors: (a) double heterostructure photodiode, and (b) *p*M*p* and (c) *n*B*p* barrier detectors.

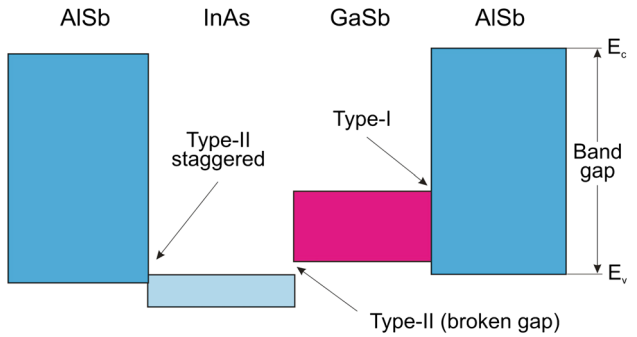

Fig. 4. Schematic of the energy band alignment in the nearly lattice-matched InAs/GaSb/AlSb material system, with three types of band alignment: type I (nested) band alignment between GaSb and AlSb, type II staggered alignment between InAs and AlSb, and type II broken-gap (or type III) alignment between InAs and GaSb (after Ref. 15).

Among the binary compounds of the 6.1-Å $A^{III}B^{V}$ family, the most popular *n*B*n* detectors are fabricated using InAs epilayers with $AlAs_ySb_{1-y}$ barriers. Theoretical predictions suggest that the valence-band offset (VBO) should be less than k_BT for barrier compositions in the range $0.14 < y < 0.18$. The second ternary alloy, with band edges near 4.2 μm, is $InAs_{1-x}Sb_x$ with barrier $AlAs_ySb_{1-y}$ grown on GaAs and GaSb substrates.[10]

The InAsSb ternary alloy is more stable in comparison with HgCdTe and has a fairly weak dependence of the band edge on composition. The stability of this material is conditioned by the stronger chemical bonds available in the lower-atomic-number $A^{III}B^{V}$ family and the larger covalent bonding contribution compared with the ionic bonding in HgCdTe.

Potential interest in InAs/GaSb T2SLs for use in the MWIR range is combined not only with advanced $A^{III}B^{V}$ molecular beam epitaxy (MBE) growth of these structures but also with the physical properties of this new artificial material that is completely different from the constituent layers. The electronic properties of SLs may be superior to those of InAsSb and HgCdTe alloys. The effective masses are not directly dependent on the bandgap energy, reducing tunneling currents in the SL in comparison with the ternary HgCdTe and InAsSb alloys. The spatial separation of electrons and holes should result in suppression of the Auger recombination rates in T2SLs. Theoretical analysis of band-to-band Auger and radiative recombination lifetimes for InAs/GaSb SLs showed that Auger recombination rates are suppressed by several orders, compared with those of bulk HgCdTe with a similar bandgap. However, the promise of Auger suppression has yet to be observed in practical device material. At the present time, the measured carrier lifetime is below 100 ns and is limited by the SRH mechanism in both MWIR and long-wavelength infrared (LWIR) compositions. It is interesting to note that InSb has had a similar SRH lifetime issue since its inspection in the 1950s.

Electron mobility approaching 10^4 cm^2/Vs has been observed in InAs/GaSb T2SLs with $<$40-Å sublayers. In the case of InAs/GaSb SL structures, the absorption is strong for normal incidence. Consequently, the SL structures provide responsivity without any need for gratings [unlike quantum-well infrared photodetectors (QWIPs)]. There is a nearly zero VBO between InAs/GaSb T2SLs (e.g., 10 ML InAs/10 ML GaSb) and $Al_{0.2}Ga_{0.8}Sb$, favoring these two materials for XBn structures. InAsPSb/B-AlAsSb devices, with longer minority-carrier lifetimes in comparison with InAs/GaSb T2SLs, are suggested for applications requiring wavelengths shorter than 4.2 μm.[25]

The main requirement which must be met to construct the XBn structure is a "zero" band offset in a proper band depending on the carrier type to be blocked. The most promising materials for nBn structures are InAs/GaSb T2SLs and InAs(InAsSb)/B-AlAsSb due to the nearly zero VBO with respect to AlAsSb barriers. Although the physical properties underline a potential superiority of T2SLs over bulk materials, there are many indicators stressing the technological problems with growth of uniform, thick SLs, resulting in low quantum efficiencies and short minority-carrier lifetimes.[26,27] Theoretical predictions place T2SLs at the forefront of IR systems development, but the greater stability over a large area, higher electron and hole mobilities, and fully developed technology favor XBn $A^{III}B^{V}$ bulk structures for HOT conditions in the MWIR range.[14] It must be stressed that the XBn architecture has also been implemented in HgCdTe, where technologically successful attempts show the prospect for circumventing the p-type doping requirements in MBE technology.[28]

HgCdTe/B-HgCdTe XBn devices operating in the MWIR range were presented by Itsuno et al.[29] The HgCdTe ternary alloy is a close-to-ideal infrared material system, conditioned by three key features: the composition-dependent tailorable energy bandgap, large optical coefficients that enable high quantum efficiency, and favorable inherent recombination mechanisms leading to long carrier lifetime and high operating temperature. These properties are a direct consequence of the energy band structure of the zincblende semiconductor. In addition, the extremely small change of lattice constant with composition makes it possible to grow high-quality layered heterostructures.

XBn DETECTOR SIMULATION PROCEDURE

Theoretical modeling of XBn detectors has been performed by numerical solution of the Poisson equation and the electron/hole current continuity equations. The commercially available APSYS platform (Crosslight Inc., Vancouver, Canada) was used in our simulation procedure. APSYS uses the Newton–Richardson method of nonlinear iteration. The applied model incorporates both electrical and optical properties to estimate device performance taking into consideration radiative (RAD), Auger, SRH GR, and band-to-band (BTB) as well as trap-assisted tunneling (TAT) mechanisms. In the TAT simulation, the Hurkx et al.[30] model was implemented. Computations were performed using Fermi–Dirac statistics for a nondegenerate semiconductor model with parabolic energy bands.[31]

The electron affinity of both the barrier layer and absorber layer seem to be the most decisive parameters to choose in XBn structure modeling. Several authors assume zero VBO between the barrier layer and active layer, while according to Vurgaftman and Klispstein, the VBO varies from 80 meV to 270 meV for the unbiased $InAs_{1-x}Sb_x/AlAs_ySb_{1-y}$ structure ($y \approx x \approx 0.09$ for GaSb substrate) at $T = 300$ K.[32] The AlSbAs electron affinity was calculated using the following dependence on the As composition: $\gamma = 3.65 - 0.15y$ eV, where $\gamma = 3.65$ eV for AlSb and $\gamma = 3.5$ eV for AlAs. The InAsSb electron affinity was assumed to be dependent on the Sb composition: $\gamma = 5.72 - 0.31x$ eV, similarly to the relation given by the IOFFE Physical Technical Institute.[33] The InAsSb/AlAsSb VBO was found to vary within the range from 4 meV to 275 meV depending on the voltage applied (calculations carried out for active-layer and barrier-layer compositions of $x = 0.09$ and $y = 0.08$, respectively). Since the AlAsSb barrier height was estimated to be $\sim$2 eV, the GR mechanism in the barrier region was found to be negligible when assessing the unipolar detector's performance. For the $Hg_{1-x}Cd_xTe$ ternary alloy, the electron affinity was calculated using the composition dependence $\gamma = 4.23 - 0.813[E_g(x,T) - 0.083]$.[34] For InAs/GaSb T2SLs and AlGaSb, the VBO was assumed to be zero.

The dependence of the energy gap and cutoff wavelength on temperature was estimated using the well-known Varshni equation.[35] The fitting parameters in the linear–quadratic Varshni relation were assumed to be equal: $E_g(0) = 0.255$ eV, $\beta = 270$ K, and $\alpha = 2.41 \times 10^{-4}$ eV/K, corresponding to literature values.[35,36]

The noise current was calculated using the following expression including thermal Johnson–Nyquist noise and electrical and background-induced shot noise:

$$i_n(V) = \sqrt{4k_BT/R + 2qI_{DARK} + 2qI_B}, \qquad (1)$$

where R is the dynamic resistance, I_{DARK} and I_B are the dark current and background-induced current, respectively, while k_B is the Boltzmann constant.

The quantum efficiency is a function of the incident radiation wavelength and current responsivity, R_i, according to the relation (without electrooptical gain):

$$R_i = \eta \frac{\lambda q}{hc}. \qquad (2)$$

The detector's detectivity is defined by the expression:

$$D^* = \frac{R_i}{i_n(V)}\sqrt{A}. \quad (3)$$

PERFORMANCE COMPARISON OF *XBn* IR DETECTORS

Figure 5 shows the performance of an optically immersed MWIR HgCdTe photodiode and InAsSb, InAs/GaSb T2SLs, HgCdTe *XBn*, and CBIRD HOT detectors. The structural parameters of the mentioned IR detectors are presented in Table I.

Properly designed, optically immersed HgCdTe devices (green solid line) approach the background-limited infrared performance (BLIP) limit [for 2π field of view (FOV)] when thermoelectrically (TE) cooled with two-stage Peltier coolers. In this case, the detectivity is proportional to n^2, where n is the refractive index (equal to 3.4 for GaAs substrates/lenses). Without optical immersion, MWIR HgCdTe photovoltaic detectors are sub-BLIP devices at T = 300 K, as *n*B*n* HgCdTe/B-HgCdTe and complementary barrier HgCdTe detectors operating at T = 200 K.

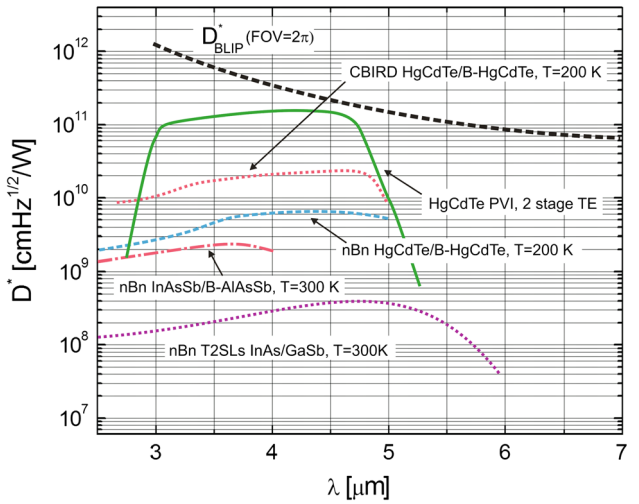

Fig. 5. Comparison of spectral detectivity of an optically immersed MWIR photovoltaic HgCdTe detector (green line after Ref. 37) versus different types of *XBn* detector: *nBn* InAs/GaSb T2SLs and *nBn* InAsSb/B-AlAsSb operated at T = 300 K; and *nBn* HgCdTe/B-HgCdTe and complementary barrier HgCdTe detectors operated at T = 200 K.

The detectivity for *n*B*n* InAs/GaSb T2SLs (10 ML/10 ML) and B-$Al_{0.2}Ga_{0.8}Sb$ is presented for T = 300 K. Maximum D^* value of 4×10^8 cm $Hz^{1/2}$/W and quantum efficiency of 15% were estimated.[36] The improvement of T2SL uniformity in the size of the constituent layers should lead to higher performance. $D^* = 2 \times 10^9$ cm $Hz^{1/2}$/W was reported for *n*B*n* InAsSb/AlAsSb detectors.[38] *n*B*n* and complementary barrier HgCdTe detectors operating in the MWIR range at T = 200 K reach detectivity of 6×10^9 cm $Hz^{1/2}$/W and 2×10^{10} cm $Hz^{1/2}$/W, respectively.[39]

CONCLUSIONS

Uncooled IR photodetectors are less well developed compared with competing thermal detectors, especially microbolometers. In the case of infrared HOT photodetectors, several new strategies have been used, including *XBn* detectors. The superior performance of the *XBn* detector in comparison with the conventional *p–n* junction photodiode is due to the fact that the *XBn* structure is not limited by generation–recombination and tunneling currents.

At the present stage, theoretical predictions place InAs/GaSb T2SLs at the forefront of IR systems development. In addition, the fully developed material technology and better stability over large areas of $A^{III}B^{V}$ favor bulk materials (e.g., InAsSb ternary alloy) for HOT conditions in the MWIR range.

The 6.1-Å family materials, such as InAsSb and InAs/GaSb T2SLs, have demonstrated the capability to provide uncooled performance comparable to that of MWIR HgCdTe photodetectors. Being grown on GaAs/GaSb substrates, these $A^{III}B^{V}$ material systems are promising for future integration with Si technology.

Further strategies for the development of *XBn* detectors should concentrate on decreasing or even removing the valence-band offset in the barrier

Table I. Structural parameters used in modeling of IR technologies presented in Fig. 5

Detector	HgCdTe PVI, two-stage TE	*n*B*n* HgCdTe/ B-HgCdTe	CBIRD HgCdTe/B-HgCdTe	*n*B*n* InAsSb/ B-AlAsSb	*n*B*n* InAs/ GaSb T2SLs
T (K)	200	200	200	300	300
Absorber, t (μm)	4	5	10	3	1.94
Absorber, N_A; N_D	6×10^{15}	10^{14}	10^{14}	6×10^{15}	6×10^{16}
Barrier, t (μm)	2	0.15	0.15	0.3	0.1
Barrier, N_A; N_D (cm^{-3})	3×10^{17}	5×10^{15}	2×10^{15}	10^{16}	5×10^{17}
Contact 1, t (μm)	10	0.16	0.16	0.25	0.15
Contact 1, N_D (cm^{-3})	10^{18}	7×10^{14}	7×10^{14}	10^{15}	10^{18}
Contact 2, t (μm)	1	–	0.4	0.1	0.15
Contact 2, N_D (cm^{-3})	10^{18}	–	10^{16}	5×10^{17}	10^{18}

layer (especially in HgCdTe *n*B*n* detectors), which will result in lower operating bias, lower dark current, and the ability to operate at higher temperatures. Ways to eliminate the valence-band offset have been proposed[40,41] and implemented for HgCdTe barrier detectors by appropriate bandgap engineering.[42]

ACKNOWLEDGEMENT

This paper has been completed under the financial support of the Polish National Science Centre (Project UMO-2012/07/D/ST7/02564).

OPEN ACCESS

REFERENCES

1. J. Piotrowski and A. Rogalski, *Infrared Phys. Technol.* 46, 115 (2004).
2. J. Piotrowski and A. Rogalski, *High-Operating Temperature Infrared Photodetectors* (Bellingham: SPIE Press, 2007).
3. G.J. Brown, *Proc. SPIE* 5783 (2005).
4. P. Martyniuk and A. Rogalski, *Opto-Electron. Rev.* 21, 239 (2013).
5. S. Maimon and G. Wicks, *Appl. Phys. Lett.* 89, 151109-1 (2006).
6. A. White, U.S. Patent No. 4,679,063, 22 September 1983.
7. G.R. Savich, J.R. Pedrazzani, D.E. Sidor, S. Maimon, and G.W. Wicks, *Proc. SPIE* 8012, 8022T (2012).
8. A. Khoshakhlagh, S. Myers, E. Plis, M.N. Kutty, B. Klein, N. Gautam, H. Kim, E.P.G. Smith, D. Rhiger, S.M. Johnson, and S. Krishna, *Proc. SPIE* 7660, 76602Z (2010).
9. E. Weiss, O. Klin, S. Grossmann, N. Snapi, I. Lukomsky, D. Aronov, M. Yassen, E. Berkowicz, A. Glozman, P. Klipstein, A. Freankel, and I. Shtrichman, *J. Cryst. Growth* 339, 31 (2012).
10. D.Z.-Y. Ting, A. Soibel, L. Höglund, J. Nguyen, C.J. Hill, A. Khoshakhlagh, and S.D. Gunapala, *Semiconductors and Semimetals*, Vol. 84, ed. S.D. Gunapala, D.R. Rhiger, and C. Jagadish (Amsterdam: Elsevier, 2011), pp. 1–57.
11. A.M. Itsuno, J.D. Philips, and S. Velicu, *J. Electron. Mater.* 40, 1624 (2011).
12. M. Kopytko and K. Jóźwikowski, *J. Electron. Mater.* 42, 3221 (2013).
13. G.R. Savich, J.R. Pedrazzani, D.E. Sidor, and G.W. Wicks, *Infrared Phys. Technol.* 59, 152 (2013).
14. P. Klipstein, *Proc. SPIE.* 6940, 69402U-1 (2008).
15. D.Z. Ting, C.J. Hill, A. Soibel, J. Nguyen, S.A. Keo, M.C. Lee, J.M. Mumolo, J.K. Liu, and S.D. Gunapala, *Proc. SPIE* 7660, 76601R-1 (2010).
16. P. Klipstein, O. Klin, S. Grossman, N. Snapi, I. Lukomsky, D. Aronov, M. Yassen, A. Glozman, T. Fishman, E. Berkowicz, O. Magen, I. Shtrichman, and E. Weiss, *Opt. Eng.* 50, 061002-1 (2011).
17. M. Reine, J. Schuster, B. Pinkie, and E. Bellotti, *J. Electron. Mater.* 42, 3015 (2013).
18. J.B. Rodriguez, E. Plis, G. Bishop, Y.D. Sharma, H. Kim, L.R. Dawson, and S. Krishna, *Appl. Phys. Lett.* 91, 043514-1 (2007).
19. B.-M. Nguyen, S. Bogdanov, S.A. Pour, and M. Razeghi, *Appl. Phys. Lett.* 95, 183502-1 (2009).
20. A.D. Hood, A.J. Evans, A. Ikhlassi, D.L. Lee, and W.E. Tennant, *J. Electron. Mater.* 39, 1001 (2010).
21. D.Z.-Y. Ting, C.J. Hill, A. Soibel, S.A. Keo, J.M. Mumolo, J. Nguyen, and S.D. Gunapala, *Appl. Phys. Lett.* 95, 023508-1 (2009).
22. J.F. Klem, J.K. Kim, M.J. Cich, S.D. Hawkins, T.R. Fortune, and J.L. Rienstra, *Proc. SPIE* 7608, 76081P (2010).
23. H. Kroemer, *Phys. E* 20, 196 (2004).
24. H. Sakaki, L.L. Chang, R. Ludeke, C.A. Chang, G.A. Sai-Halasz, and L. Esaki, *Appl. Phys. Lett.* 31, 211 (1977).
25. F. Kelm, S.D. Hawkins, J.K. Kim, D. Leonhardt, and E.A. Shaner, *J. Vac. Sci. Technol.* B31, 03C115-1 (2013).
26. D. Donetsky, G. Belenky, S. Svensson, and S. Suchalki, *Appl. Phys. Lett.* 97, 052108 (2010).
27. S. Myers, E. Plis, C. Morath, V. Cowan, N. Gautam, B. Klein, M.N. Kutty, M. Naydenkov, T. Schuler-Sandya, and S. Krishna, *Proc. SPIE* 8155, 815507-1 (2011).
28. S. Velicu, J. Zhao, M. Morley, A.M. Itsuno, and J.D. Philips, *Proc. SPIE* 8268, 82682X (2012).
29. A.M. Itsuno, J.D. Philips, and S. Velicu, *Appl. Phys. Lett.* 100, 161102 (2012).
30. G.A. Hurkx, D.B.M. Klaassen, and M.P.G. Knuvers, *IEEE Trans. Electron Devices* 39, 2 (1992).
31. APSYS Macro/User's Manual ver. 2011, Crosslight Software, Inc., 2011.
32. I. Vurgaftman, J.R. Meyer, and L.R. Ram-Mohan, *J. Appl. Phys.* 89, 5815 (2001).
33. http://www.ioffe.ru/SVA/NSM/Semicond/InAsSb/basic.html.
34. P.P. Capper, *Properties of Narrow Gap Cadmium-Based Compounds* (London: The Institution of Electrical Engineers, 1994).
35. B. Klein, E. Plis, M.N. Kutty, N. Gautam, A. Albrecht, S. Myers, and S. Krishna, *J. Phys. D Appl. Phys.* 44, 075102 (2011).
36. J. Wróbel, P. Martyniuk, E. Plis, P. Madejczyk, W. Gawron, S. Krishna, and A. Rogalski, *Proc. SPIE* 8353, 8353-16 (2012).
37. http://www.vigo.com.pl/.
38. P. Martyniuk and A. Rogalski, *Proc. SPIE* 8704, 87041X (2013).
39. P. Martyniuk and A. Rogalski, *Solid-State Electron.* 80, 96 (2013).
40. E.F. Schubert, L.W. Tu, G.J. Zydzik, R.F. Kopf, A. Benvenuti, and M.R. Pinto, *Appl. Phys. Lett.* 60, 466 (1992).
41. S.D. Gunpala, D.Z. Ting, C.J. Hill, and S.V. Bandara, U.S. Patent No. 7,737,411, 2010.
42. N.D. Akhavan, G. Jolley, G. Umana-Membreno, J. Antoszewski, and L. Faraone, *Extended Abstracts*, The 2013 Workshop on the Physics and Chemistry of II–VI Materials, Chicago (2013).